ASEAN Engineering Journal

Full Paper

THE EFFECT OF NACL ADDITION TO TiO_2/NiSe/NC PHOTOCATALYTIC FOR HYDROGEN GAS PRODUCTION

Tiara Ardianti, Yuly Kusumawati*

Departement of Chemistry, Faculty of Science and Data Analytics, Institut Teknologi Sepuluh Nopember, Kampus ITS Keputih, Sukolilo, Surabaya, 60111, Indonesia

Article history
Received
30 September 2023
Received in revised form
03 January 2024
Accepted
04 January 2024
Published online
31 August 2024

*Corresponding author
y_kusumawati@chem.its.ac.id

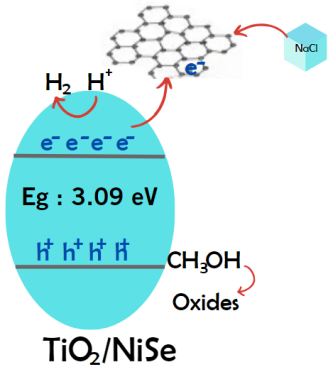

Abstract

The widespread utilization of fossil fuel has resulted in fuel scarcity due to population growth and increased industrialization, driving the evolution of new renewable energy sources (NRE**).** Alternatively, hydrogen production through solar water splitting and TiO_2 as a potential photocatalyst can be developed due to its good stability, environmental friendliness, and economic viability. However, TiO_2 has the disadvantage of a wide bandgap that requires high energy and fast recombination. Therefore, in this research, TiO_2/NiSe (TN) was synthesized with N doped carbon dopant modified with NaCl as a photocatalyst material through a solvothermal method. The characterized material using XRD, SEM, UV-DRS, BET, and FTIR. Photocatalytic activity tests were conducted to determine hydrogen production using an MQ8 sensor integrated with an Arduino microcontroller system. The synthesized materials are TN, TNC-0, and TNC-10. The addition of NaCl in carbon doped nitrogen materials of photocatalyst TNC-10 shows a reduction of the bandgap that is the lowest bandgap value obtained was 3.09eV. The photocatalytic activity test results showed a hydrogen production of 120 ppm for TNC-10, which is six-times higher compared to bare TiO_2 as a photocatalyst. The increase in hydrogen gas production is due to the addition of NaCl to NC, which can enhance the photocatalytic activity and hydrogen adsorption on the catalyst surface during hydrogen production.

Keywords: Photocatalytic H_2 production, NaCl, NiSe, TiO_2, water splitting, Energy research

1.0 INTRODUCTION

The global energy landscape has long been dominated by conventional fossil fuels, but their overreliance has led to issues such as resource depletion and harmful emissions. The combustion of fossil fuels releases harmful pollutants into the atmosphere, posing significant threats to human health[1]. In response to these pressing challenges, hydrogen possesses an energy density three times higher than the gasoline, rendering it an attractive option for a wide range of applications [2]. Generally, hydrogen production has relied heavily on petrochemical methods, such as steam methane reforming, which relies on natural gas. However, these methods are considered environmentally unfriendly due to their significant emissions of hazardous gases, particularly CO_2. Therefore, water splitting method that utilizes solar energy get considerable interest as a more sustainable of hydrogen evolution [3]. Photocatalysis is a key process in solar-driven water splitting, involving materials that exhibit catalytic activity upon exposure to electromagnetic radiation, typically within the UV to near-visible light spectrum [4]. Over the years, numerous photocatalysts, including TiO_2, ZnO, CdSe, NiO, and ZnSe, have been extensively studied for their potential in photocatalytic hydrogen generation [5]. Nevertheless, the quest for an efficient photocatalyst that possesses the right band gap, cost-effectiveness, non-toxicity, and enhanced stability for water splitting reactions continues to be a focal point of research and development [6].

Titanium dioxide (TiO_2) has long been garnered acknowledgment as a central material in the domain of

photocatalysis. This recognition is attributable to its distinctive attributes, including a broad bandgap and a valence band located above the necessary potential level for water oxidation [7]. Nonetheless, its potential for achieving efficient photocatalytic hydrogen production remains limited. [8]. Recombination of photogenerated charge carriers, including holes and electrons, is the main factor limiting TiO_2 ability to function as a photocatalyst [7]. Photocatalytic hydrogen production occurs when incoming photons with energy exceeding the photocatalyst's bandgap create electron-hole pairs. Addressing the recombination issue is essential for boosting the efficiency of this process [9]. Co-catalyst systems have emerged as a promising avenue for achieving efficient photocatalytic hydrogen production. Notably, noble metals like Pt, Ir, Ru, and Rh have yielded encouraging results in this regard. Nevertheless, their limited accessibility and elevated expenses have restricted their extensive deployment [10]. Consequently, extensive research efforts have been directed towards identifying alternative non-noble metal co-catalysts that can deliver economically superior hydrogen production rates [11]. Chalcogenides, have garnered attention as potential co-catalysts. They offer advantages such as high dispersibility, active sites, and small size, facilitating effective absorption of H^+ ions from the solution for reduction by electrons [11].

Chalcogenide metals are currently regarded as promising candidates [12], among these metals, selenides exhibit superiority owing to their enhanced electrical conductivity in comparison to other oxides and sulfides. Remarkably, the synthesis of nickel-based selenides is distinguished by its cost-effectiveness and reduced toxicity in comparison to cadmium selenides [13]. NiSe crystals modified with the photocatalyst Mn0.5Cd0.5S, synthesized using a solvothermal method at 180°C for 24 hours, exhibit significantly higher hydrogen (H_2) production activity compared to pure Mn0.5Cd0.5S. This improvement can be ascribed to the enhanced separation and extended lifetime of photoexcited electrons. [14]. In a study conducted by Zhen and colleagues in 2018, it was observed that the photocatalyst of NiSe/MnO_2-CdS generated a higher quantity of H_2 gas compared to Pt/MnO_2-CdS, indicating that NiSe may have the ability to replace noble metals in enhancing photocatalytic activity in photocatalysts. The formation of a heterojunction semiconductor between TiO_2 and NiSe has been proven to reduce the bandgap, thereby enhancing photocatalytic activity [15].

NiSe exhibits certain weaknesses in its properties, as evidenced by the lower H_2 production activity of TiO_2/NiSe compared to TiO_2/Pt. This can be attributed to NiSe poor thermal stability, tendency to agglomerate, and limited active sites for hydrogen production [15]. Research conducted by Ding and colleagues in 2019 successfully modified NiSe using nitrogen-doped carbon materials, which can reduce agglomeration while improving conductivity and thermal stability [16]. The inclusion of a porous structure within the catalyst affords an extensive surface area, thereby promoting increased interaction between adsorbate molecules and the catalyst. Furthermore, it facilitates the diffusion of molecules as well as the transfer of photo charge. Mesoporous carbon structures feature one-dimensional open-channel structures conducive to enhancing diffusion rates [17].

Nitrogen-doped carbon can be synthesized using chitosan due to its high nitrogen content [18]. To produce nitrogen-doped carbon with a mesoporous structure, using carbon activator such as sodium chloride (NaCl) require carbonization process at a high temperature, typically 900°C. NaCl has mobile liquid, will explore and etch the carbon matrix at carbonization temperatures above 801°C, which will cause the collapse of porous carbon pore structures. [22]. The presence of NaCl, along with thermal energy, can drive the transformation of irregular carbon into structured carbon and enhance electrical conductivity [19].

In this research, the TiO_2/NiSe photocatalytic material was modified by introducing nitrogen-doped carbon (NC). The resulting material was confirmed through a series of characterizations, including UV-DRS, XRD, FTIR, BET, and SEM-EDS. Additionally, photocatalytic activity tests were conducted to assess the hydrogen production performance. The modification of TiO_2/NiSe/NC aims to reduce the bandgap, increase the surface area, and enhance photocatalytic activity and used as a photocatalyst to produce hydrogen fuel by water splitting in order to accomplish this.

2.0 METHODOLOGY

2.1. Material and Methods

The equipment utilized in this research comprised of magnetic stirrer, ultrasonicator, teflon-based autoclave, tube furnace, centrifugation device (Hettich Universal 320), photocatalytic reactor setup, UV-LED lamp (EPILEDS, 12 watts, λ = 365nm), UV box, hydrogen sensor MQ8, and Arduino microcontroller. Characterization instruments included X-Ray Diffraction (XRD-Philips PW1140/90), Scanning Electron Microscopy (SEM-HITACHI FLEXSEM 100), UV-Diffuse Reflectance Spectrophotometer (UV-DRS - SHIMADZU), Fourier Transform Infrared Spectroscopy (FTIR-SHIMADZU), and Brunauer Emmett Teller (BET- Micromeritics Tristar II Plus 3020). The materials used in this study encompassed chitosan, titanium dioxide (TiO_2), nickel (II) sulfate hydrate ($NiSO_4.6H_2O$), sodium selenite (Na_2SeO_3), ethylene glycol, ethanol, methanol, ice cubes, and deionized water.

In this study, several stages were undertaken, beginning with the synthesis of nitrogen-doped carbon (NC) from chitosan with the addition of NaCl to the carbon [20]. The composite of TN was then synthesized in combination with NC. Here the various sample modifications were employed in this research, as detailed in Table 1.

Table 1 The Variation of sample

No.	Materials	Sample's Name
1	NC	NC-0
2	NC + NaCl	NC-10
3	TiO_2 + NiSe	TN
4	TiO_2 + NiSe + NC	TNC-0
5	TiO_2 + NiSe + NC + NaCl	TNC-10

The synthesis of NC was carried out using the hydrothermal method [21]. Deionized water was mixed with solid NaCl before being used to dissolve 2 grams of chitosan. In this stage, variations in the amount of added NaCl were 0 and 10 grams per 35 mL of aquades. The chitosan powder was added to the NaCl solution and conduct ultrasonication for 30 minutes. Subsequently, a hydrothermal process was conducted at 220°C [22] for 6 hours. The resulting solid was centrifuged several

times with deionized water and ethanol, and then dried at 80°C for 24 hours.

The TN composite was synthesized using the solvothermal method adapted from the study by Gong et al. (2019). A total of 400 mg of TiO_2 powder, 290.58 µmol of $NiSO_4 \cdot 6H_2O$, and Na_2SeO_3 were dissolved in 40 mL of glycol. The mixture was transferred into autoclave and kept at 180°C for 24 hours. The resulting solid material was centrifuged, washed multiple times with deionized water, and absolute ethanol, and then dried.

TiO_2/NiSe/NC was synthesized 400 mg of TN powder and 18.75 mg of NC powder were dissolved in 40 mL of glycol and stir. The mixture initially showed black carbon powder that didn't dissolve completely, prompting a 30-minute ultrasound treatment inside a autoclave to ensure full dissolution of TN and NC. The autoclave kept at a temperature of 180°C for 24 hours. The resulting solid material washed multiple times using aquades and ethanol, and then dried.

2.2. Characterization

The materials obtained in this research will undergo characterization using various techniques: The X-ray diffraction patterns for the synthesized solid materials will be recorded using an X-ray diffractometer with Cu Kα radiation (λ = 1.54060 Å). The analysis will cover angles between 5-90° with an acceleration voltage of 40 kV and a current of 30 mA. Scanning Electron Microscope (SEM) will be used to characterize using HITACHI FLEXSEM 100. UV-Diffuse Reflectance Spectrophotometer (UV-DRS) will be performed using a Shimadzu UV-2450 spectrophotometer with a wavelength range of 200-800 nm. Fourier Transform Infrared Spectroscopy (FTIR) using a Shidamazu FTIR 8400S instrument will be utilized to identify the types and presence of functional groups in the solid materials. Sample preparation will involve mixing the synthesized material with KBr in a 1:10 ratio. BET Analysis involving both degassing and analyzing, will be using Micromeritics Tristar II Plus 3020 to calculate the pore distribution and specific surface area.

2.3. Photocatalytic Test

The photocatalyst solid weighs a mass of 0.1 grams then dissolved in a mixture of 20 mL of methanol and 80 mL of deionized water within the photocatalytic reactor tube. The reactor tube is placed on top of a chamber filled with ice cubes inside a UV box. The photocatalytic water splitting test is conducted under the illumination of 2 UV-LED lamps (EPILEDS, 12 watts, λ = 365nm). This setup allows for controlled experimentation to assess the photocatalyst water splitting activity, generating hydrogen under UV irradiation.

3.0 RESULTS AND DISCUSSION

The X-ray diffraction (XRD) analysis of the sample was conducted within the angular range of 2θ 0-90°, employing a Cu Kα X-ray source with a wavelength (λ) of 1.54060 Å. The diffractogram pattern of the TiO_2 sample in figure 1 reveals distinct diffraction peaks at 2θ. These observed peaks correspond to crystallographic planes (101), (004), (200), (105), (211), (204), and (215), respectively, indicating the presence of the TiO_2 anatase phase. This identification is assigned to crystallographic planes to JCPDS reference code 99-0008.

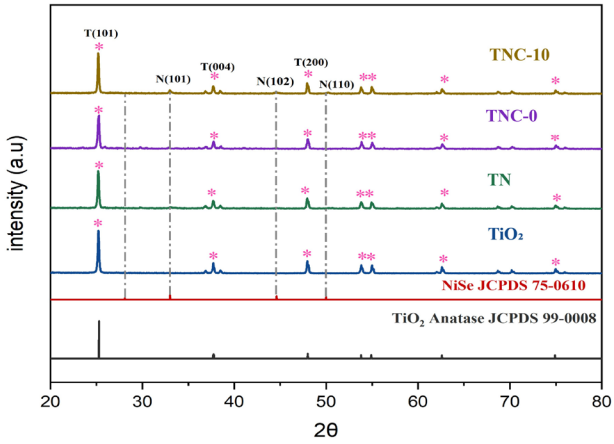

Figure 1 XRD pattern of TN with different amounts of loading NaCl

The XRD pattern of the TN sample is presented in Figure 4.4. The diffraction results reveal distinct and well-defined peaks at 2θ values of 25.3°, 37.8°, and 48.0°. These peaks are assigned to the crystallographic planes (101), (004), and (200), respectively, indicating the presence of the TiO_2 anatase phase. This observation aligns with the reference code JCPDS 99-0008, as reported by Zheng et al. in 2016 [23]. Additionally, a peak at 2θ = 27.4° originating from the crystallographic plane (110) is observed, confirming the presence of the TiO_2 anatase phase according to JCPDS 99-0090 [25]. The pattern of TiO_2 also indicates that the TiO_2 lattice structure remains stable in high temperature. Furthermore, distinct diffraction peaks at 2θ values of 33.0°, 44.6°, and 49.9°, corresponding to the crystallographic planes (101), (102), and (110), respectively, are evident, confirming the presence of the NiSe phase in the sample, consistent with JCPDS 75-0610. The XRD patterns of TNC-0 and TNC-10 are also shown in Figure 1. Similar to the TN sample, both patterns exhibit clear diffraction peaks at 2θ values of 25.3°, 37.8°, and 48.0°, corresponding to the crystallographic planes (101), (004), and (200), indicative of the TiO_2 anatase phase in accordance with JCPDS 99-0008, as reported by Zheng et al. in 2016. Moreover, in the TNC-10 pattern, distinct and well-defined diffraction peaks at 2θ values of 33.0°, 44.6°, and 49.9° are prominently visible, originating from the crystallographic planes (101), (102), and (110), respectively. These peaks confirm the presence of the NiSe phase, consistent with JCPDS 75-0610. The XRD analysis establishes that the synthesized NiSe in both TN and TNC-10samples is of pure phase. The XRD diffractogram of the samples additionally reveals broad and weak peaks at 2θ = 25°, corresponding to the crystallographic plane (002) indicative of a carbon lattice structure.

The BET characterization was conducted to confirm the specific surface area (SSA) and pore size distribution. N2 adsorption-desorption isotherms for N-doped carbon (NC) samples, namely NC-0 and NC-10, exhibited Type-IV isotherms, as depicted in Figure 2. At low relative pressures (P/P0 = 0.05), there was a pronounced adsorption, and clear hysteresis loops within the range of P/P0 from 0.4 to 0.9 were observed for all samples. These findings indicate the coexistence of highly developed micropores and mesopores [24]. As shown in Figure 2, the PSD curves reveal that both NC samples, with or without

the addition of NaCl, possess hierarchically porous structures with broad pore size distributions.

Table 2 BET Analysis

Sampel	NC-0	NC-10
Single point surface area at P/Po (m^2/g)	177,4493 m^2/g	710,7046 m^2/g
BET Surface Area (m^2/g)	180,2319 m^2/g	680,5293 m^2/g
Pore Volume (cm^3/g)	0,239201 cm^3/g	0,462685 cm^3/g
Adsorption average pore diameter (nm)	5,3087 nm	2,7196 nm
Desorption average pore diameter (nm)	4,7439 nm	2,5274 nm

Comparing the NC-0 and NC-10 samples reveals notable differences in pore volume within the 4.744 nm size range, as presented in Table 2 Specifically, NC-0 exhibits a significantly higher pore volume of 4.744 nm with a relatively low SSA of 180.2319 m^2/g and a pore volume of 0.239 cm^3/g. Conversely, NC-10 displays the lowest pore volume within the 2.52 nm range but boasts a considerably higher SSA of 680.53 m^2/g and a pore volume of 0.463 cm^3/g. The addition of NaCl to NC-10 sample indicates that it possesses a higher SSA compared to NC-0, which was synthesized at the same carbonization temperature, and yields more pores due to the catalytic activation by NaCl. This finding confirms the role of NaCl in pore structure formation during carbonization [25]. We can infer that NaCl acts as a pore-forming agent. From the isotherm curves in Figure 2, it can be inferred that the material is mesoporous, which is further supported by the pore diameter results exceeding 2 nm [24].

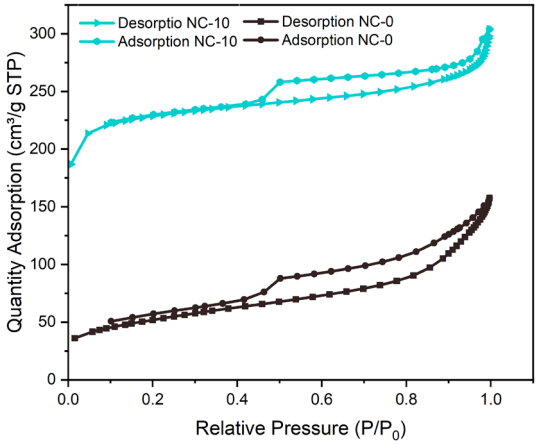

Figure 2 N_2 adsorption-desorption isotherms of NC-10 and NC-0

The morphology of the samples was investigated using SEM examination, and particle sizes were measured. The SEM image in Figure 3 (a) shows the morphology of N-doped carbon (NC) with the addition of 10 grams of NaCl after carbonization at 900°C, revealing several distributed pores within the nanometer size range. SEM measurements at a magnification of 50,000kv yielded an average pore diameter of 103 nm. The surface of NC exhibits a sponge-like appearance with an open and porous structure that supports the formation of larger particles. The addition of NaCl to carbon has a catalytic effect on porous carbon. Meanwhile, N doped porous carbon is created because of the high-temperature procedure, which guarantees that nitrogen atoms (from amino groups) are incorporated into the carbon structure [26].

Figure 3 (b) shows SEM images of TN with an average crystal diameter of 197.5 nm. Figure 3 (c) displays SEM images of TNC-0 with an average crystal diameter of 229.56 nm, indicating a heterogeneous morphological structure similar to TN. SEM images of TNC-0 and TNC-10 suggest a homogeneous surface morphology, indicating that the NC dopant particles can be well-dispersed on TN without agglomeration. Diameter measurements using ImageJ software for TNC-10, as shown in Figure 3 (d), reveal an average crystal diameter of 203.08 nm.

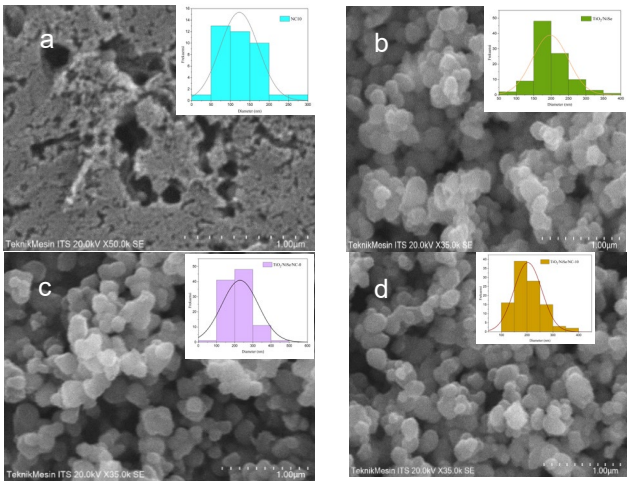

Figure 3 SEM image of (a) NC-10 (b) TN (c) TNC-0 (d) TNC-10

Based on the SEM micrographs obtained, it can be concluded that the method of introducing nitrogen-doped carbon (NC) into TN has an impact on the particle size and morphology after calcination, resulting in larger particle diameters compared to the undoped counterpart. The addition of 10 grams of NaCl to NC in TN reduces the particle size, although not significantly. The selenization process leads to the reaction of nickel with selenium, forming smaller particles [27]. However, the addition of NC-0 and NC-10 dopants during the synthesis of TN disrupts the selenization process, resulting in larger particle sizes. Particle size is also influenced by the type of dopant added to TN. The addition of NC dopant with NaCl has been shown to yield smaller particle sizes compared to the addition of NC dopant to TN. The reduction in crystal size also confirms the absence of agglomeration [28].

The results of EDS analysis, as presented in Figure 4, indicate the successful synthesis of TN modification with the addition of NC and NaCl. This is evident in the TNC-10 sample, where peaks detect the presence of elements Ti, O, C, N, as well as trace amounts of Ni and Se are observed. The Ti and O elements originate from solid TiO_2, which is the primary photocatalytic material in the photocatalytic process. Nitrogen and carbon elements are derived from chitosan, with carbon and nitrogen reacting to form stable active centers during the doping process. The Ni element arises from the precursor $Ni(NO_3)_2{\cdot}6H_2O$, and Se originates from the selenization process involving the precursor Na_2SeO_3. In conclusion, it can be inferred that the addition of 10 grams of NaCl to NC in TN enhances the percentage of Ni and Se elements present

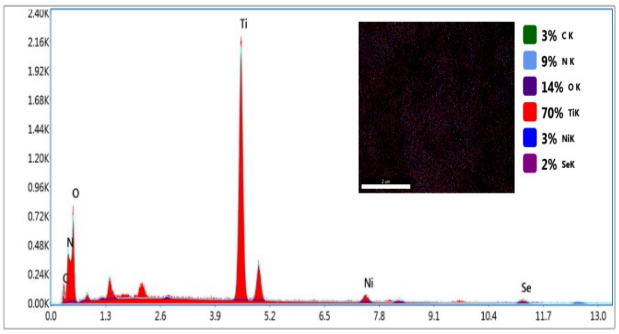

Figure 4 EDX of TNC-10

Figure 5 illustrates how FTIR spectroscopy was used to identify changes in the functional makeup of the materials. Broad bands with a center of 3420 cm^{-1} are visible in the FTIR spectra of nitrogen-doped carbon, NC-0, and NC-10. These broad bands correspond to the stretching vibrations of O-H bonds in hydroxyl and carboxyl groups, as well as adsorbed water, which also overlaps with the N-H bond vibrations [29]. The stretching vibration of C-N bonds is detectable at 1445 cm^{-1}. A minor peak at 880 cm^{-1} observed in the N-C spectrum originates from the C-O-C bond [30]. Aliphatic C-H bond vibrations are present in the absorption region at 2920 cm^{-1}, and a peak at 2850 cm^{-1} indicates O-CH_3 bonding. In NC-10, there is a noticeable N-H bond at 1520 cm^{-1} that is not present in NC-0. The functional groups observed in the FTIR spectra of NC-0 and NC-10 align with the functional groups of nitrogen-doped carbon in previous research [24].

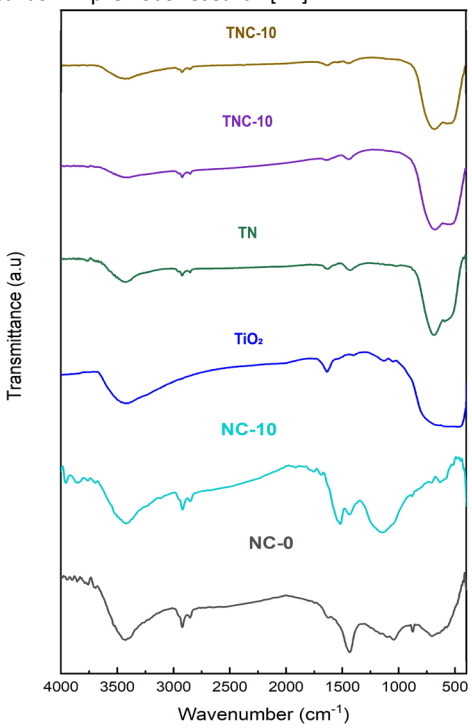

Figure 5 FTIR spectrum of NC-0, NC-10, TiO_2, TN, TNC-0, and TNC-10

The spectral analysis of bare TiO_2 reveals a pronounced absorption pattern within the wavelength range of 800-400 cm^{-1}, primarily attributed to Ti-O stretching and Ti-O-Ti bonding. These absorption peaks signify the presence of the anatase crystal structure in TiO_2. Furthermore, the TiO_2 surface is characterized by the presence of abundant hydroxyl groups, and the presence of small crystalline entities can contribute to the broadening of these peaks. Specifically, spectroscopic bands are discerned at approximately 3391.72 cm^{-1}, assigned to both symmetric and asymmetric stretching vibrations of hydroxyl groups (Ti-OH). Additionally, a distinctive peak at 1627.28 cm^{-1} is associated with the vibrations of O-H groups stemming from adsorbed water molecules. The broad absorption band spanning from 450 to 800 cm^{-1} is linked to vibrational modes originating from Ti-O-Ti bonds within the TiO_2 nanoparticles. In accordance with established TiO_2 spectra, the peak at 463.88 cm^{-1} can be attributed to Ti-O bonding vibrations within the anatase TiO_2 lattice. Finally, the infrared absorption band appearing at 728.77 cm^{-1} is ascribed to the stretching vibrations of Ti-O-Ti bonds.[31].

The FTIR spectrum of TN displays a signal at approximately 669.31 cm^{-1}, attributed to the vibration of nickel selenide bonds, consistent with the FTIR spectrum generated [16]. The FTIR spectrum of TN exhibits absorption peaks in the range of 1000 to 400 cm^{-1}, originating from Ti-O stretching vibrations. Peaks within the 400-800 cm^{-1} range indicate the presence of anatase-phase TiO_2. The peak at 453.29 cm^{-1} indicates Ti-O bonding vibrations, and the IR absorption band at 792.77 cm^{-1} indicates Ti-O-Ti stretching vibrations [5] (Wang et al., 2016). Both the FTIR spectra of TNC-0 and TNC-10 exhibit absorption peaks at around 459.07 cm^{-1}. This can explain to the presence of the Ti-O functional group, and at 1433.16 cm^{-1}, indicating the presence of the C-N functional group in nitrogen-doped carbon. However, there is no observable Ni-Se absorption peak at around 669.31 cm^{-1}, as seen in the NiSe/NC spectrum. This could be due to the low selenium content during the synthesis stage, rendering the Ni-Se functional group less conspicuous during FTIR characterization.

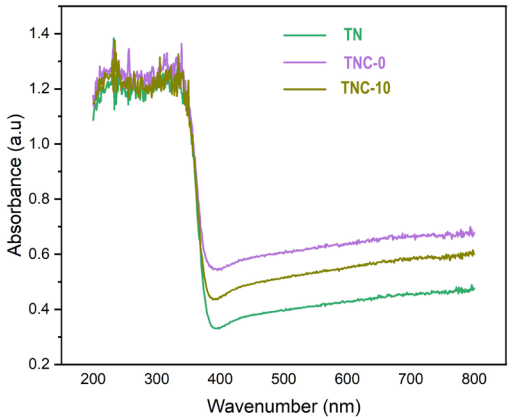

Figure 6. The absorbance of the TN, TNC-0, and TNC-10

The optical properties and band gap were analyzed using Ultraviolet Diffuse Reflectance Spectroscopy. The purpose of this UV-DRS testing was to determine the semiconductor band gap and the wavelength of light absorption, which influences the semiconductor's electron excitation performance. In the case of pure TiO_2, it has a band gap of 3.2 eV with an absorption wavelength of 380 nm, making it active in the UV-A region [15]. The addition of NC-0 and NC-10 to TN results in strong absorbance in the 380-400 nm wavelength range, as shown in Figure 6, which is a characteristic absorbance of TiO_2.

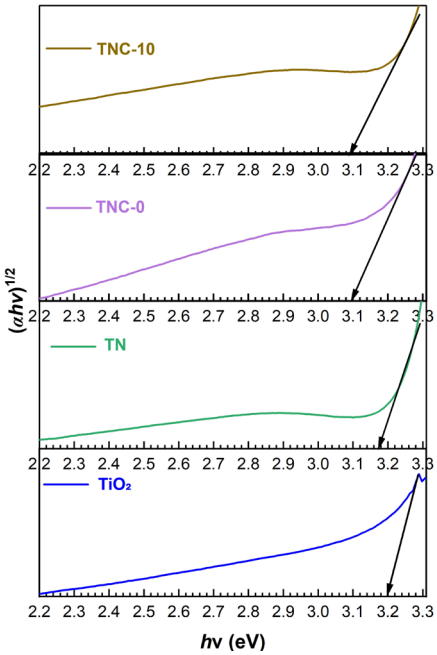

Figure 7. The band gap of the TN, TNC-0 and TNC-10

The synthesized photocatalyst can exhibit photocatalytic activity in the UV region because the material has an energy band gap that allows electron to excite from the valence band to the conduction band when exposed to sufficient energy. The results of the band gap energy analysis for the samples are presented in Figure 7, where the band gaps for TN, TNC-0, and TNC-10 are 3.18, 3.1, and 3.09 eV, respectively. The lowest band gap value is obtained for TNC-10, which is 3.09 eV. This 3.09 eV band gap corresponds to the wavelength of violet light 401.294 nm [30]. the synthesized photocatalyst can exhibit photocatalytic activity in the UV region because the material has an energy band gap that allows electron to excite from the valence band to the conduction band when exposed to sufficient energy. The obtained band gap values indicate that the addition of NiSe and NC to TiO_2 can decrease the band gap, while the addition of NaCl to NC in TN increases the band gap. This is because the band gap is primarily influenced by NiSe, which has a band gap of 2.01 eV. The addition of NaCl to carbon functions to enhance the active sites of the photocatalyst. The UV-LED lamp used has a wavelength of 365 nm, which, when converted, corresponds to a photon energy value of 3.396 eV. A smaller band gap energy results in lower energy required for electrons in the valence band to undergo excitation to the conduction band, enabling photocatalytic activity to occur.

Photocatalytic hydrogen activity testing was conducted under UV-LED irradiation to compare the photocatalytic performance of TiO_2, TN, TNC-0, and TNC-10, with and without the addition of NC. The average production of hydrogen, measured in parts per million (ppm), was recorded as an output signal from the Arduino Uno microcontroller. Pure TiO_2 exhibited an average hydrogen production of 17.87 ppm. Similarly, the average hydrogen production by TN was 41.4 ppm. The addition of nitrogen-doped carbon to TN significantly increased the average hydrogen production after 20 minutes of irradiation. The average hydrogen production by TNC-0 and TNC-10 was 60 and 120 ppm, respectively, as shown in Figure 8. TNC-10 generated seven times more hydrogen gas compared to bare TiO_2.

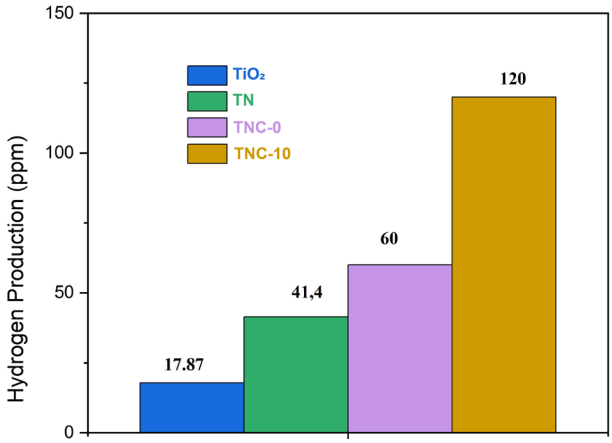

Figure 8. Hydrogen evolution activity over TiO_2, TN, TNC-0 and TNC-10

The addition of NaCl to NC in TN influenced enhancing the active sites, leading to increased hydrogen production from TNC-0. Although the addition of NaCl did not significantly reduce the band gap of the photocatalyst, it improved the conductivity of the photocatalyst according the research that conduct by Liu 2022 [26], which enhances mass transfer and hydrogen adsorption on the catalyst surface during hydrogen production. When TN was combined with NC-10, the rate of hydrogen production increased significantly due to the electric field formed at the TiO_2, NiSe, and NC-10 heterojunction. The increased H_2 generation activity of the composite was attributed to the alignment of the conduction and valence band energy positions of TiO_2, NiSe, and NC-10 for charge transfer mechanisms, increased specific surface area, facilitating efficient electron and hole transfer mechanisms.

Based on the previously discussed results, the photocatalytic water splitting mechanism enabled by TiO_2/NiSe/NC can be depicted in Scheme Figure 8. Photocatalytic activity testing performed under UV-visible light simultaneously generates electron-hole pairs in both TiO_2 and NiSe/NC. Pure TiO_2 without a cocatalyst is known to have a conduction band potential of -0.31 V, which is more negative than the value of 0.0 V, representing the H^+/H_2 reduction potential. However, pure TiO_2 can only produce hydrogen evolution in small quantities due to rapid recombination of photoexcited electron-hole pairs and a large hydrogen production overpotential [32]. Referring to Zhang et al. (2010), NiSe as a cocatalyst has a more positive conduction band potential compared to TiO_2, which is -0.16 V. This value is closer to the hydrogen reduction potential and the presence of hydrogen production overpotential. Therefore, pure NiSe cannot efficiently drive photoexcited electrons to reduce H^+ into hydrogen. This is also supported by research conducted by Gong et al. (2019), where pure NiSe can only produce hydrogen evolution in insignificant amounts. In this research, NiSe was added to narrow the band gap of TiO_2, and carbon and nitrogen doping was employed to enhance the stability and surface area of the photocatalytic material. The modification of TN with carbon and nitrogen doping creates an internal electric field at the phase interface, which can drive photo-generated electrons from the TiO_2 conduction band towards NiSe. In the photocatalytic activity testing conducted,

methanol was used as a sacrificial agent to enhance hydrogen evolution. The presence of a sacrificial agent, in this case, methanol, captures electrons in the TiO_2 valence band and transfers them to NiSe, where they are captured by electron donors. Simultaneous electron transfer from TiO_2 to NiSe and NiO, along with significant hole capture, can prevent the recombination of electron-hole pairs in TiO_2 [15].

4.0 CONCLUSION

The addition of activated carbon, represented by NaCl, into the nitrogen-doped carbon matrix of TN photocatalysts aimed at boosting hydrogen production, has been achieved successfully. The modification of nitrogen-doped carbon with NaCl within TNC-10 has shown promising results in enhancing photocatalytic performance. NaCl was integrated into the nitrogen-doped carbon structure to assess its impact on the hydrogen evolution photocatalytic activity. In the various photocatalyst samples, encompassing TN, TNC-0, and TNC-10, band gap measurements revealed values of 3.18, 3.1, and 3.09, respectively. This indicates that the band gap of the photocatalyst was narrowed to the visible light spectrum. Importantly, the addition of NaCl did not lead to a significant reduction in the band gap. Photocatalytic testing for water splitting demonstrated that the incorporation of NaCl into the TNC-10 photocatalyst resulted in a higher yield of hydrogen compared to TiO_2, TN, and TNC-0. Based on the research findings, the TNC-10 variation displayed the most optimized performance. Specifically, TNC-10 exhibited the narrowest band gap at 3.09 eV, and it yielded an average hydrogen production rate of 120 ppm. This performance represented a remarkable seven-fold increase relative to pure TiO_2. These advancements in performance were attributed to the presence of NiSe as a cocatalyst compound, effectively inhibiting the rapid recombination of electron-hole pairs within the photocatalytic material. Additionally, NC-10 enhanced stability, pore distribution, and surface area, thus improving the evolution of hydrogen gas. In summary, these findings suggest that TNC-10 holds substantial potential for practical applications and further development as a photocatalytic agent for the process of water splitting to produce hydrogen.

Acknowledgement

The Deputy for Research and Development, Ministry of Research and Technology of Republic Indonesia the research funding PKDN scheme No 1968/PKS/ITS/2023.

References

[1] K. C. Christoforidis and P. Fornasiero, 2017. "Photocatalytic Hydrogen Production: A Rift into the Future Energy Supply," *Chemistry Catalytic Europe* 9(9): 1523–1544, doi: 10.1002/cctc.201601659.

[2] H. Ahmad, S. K. Kamarudin, L. J. Minggu, and M. Kassim, 2015, "Hydrogen from photo-catalytic water splitting process: A review," *Renew. Sustainable Energy Review.*, 43: 599–610, doi: 10.1016/j.rser.2014.10.101.

[3] N. L. D. Silva *et al.*, 2018. "Superior solar-to-hydrogen energy conversion efficiency by visible light-driven hydrogen production via highly reduced Ti^{2+}/Ti^{3+} states in a blue titanium dioxide photocatalyst," *Catal Science Technology* 8(18): 4657–4664. doi: 10.1039/C8CY01212A.

[4] D. V. Wellia, Y. Kusumawati, L. J. Diguna, N. Pratiwi, R. A. Putri, and M. I. Amal, 2020, "*Mesoporous Materials for Degradation of Textile Dyes,*" 255–288. doi: 10.1007/978-3-030-16427-0_10.

[5] H. Wang, W. Chen, J. Zhang, C. Huang, and L. Mao, 2015 "Nickel nanoparticles modified CdS – A potential photocatalyst for hydrogen production through water splitting under visible light irradiation," *Internation Journal Hydrogen Energy* 40: 340–345. doi: 10.1016/j.ijhydene.2014.11.005.

[6] L. Lin, T. Hisatomi, S. Chen, T. Takata, and K. Domen, 2020 "Visible-Light-Driven Photocatalytic Water Splitting: Recent Progress and Challenges," *Trends Chemistry*. 2(9): 813–824. doi: 10.1016/j.trechm.2020.06.006.

[7] R. Zouzelka, Y. Kusumawati, M. Remzova, J. Rathousky, and T. Pauporté, 2016, "Photocatalytic activity of porous multiwalled carbon nanotube-TiO_2 composite layers for pollutant degradation," *Journal. Hazardous Material*, 317: 52–59, doi: 10.1016/j.jhazmat.2016.05.056.

[8] P. Ravi, V. Navakoteswara Rao, M. V. Shankar, and M. Sathish, 2020, CuO@NiO core-shell nanoparticles decorated anatase TiO_2 nanospheres for enhanced photocatalytic hydrogen production," *International Journal Hydrogen Energy*, 45(13): 7517–7529, doi: 10.1016/j.ijhydene.2019.05020.

[9] J. Wang *et al.*, 2020, "Synergistic effects of nano-silica and fly ash on properties of cement-based composites," C*onstruction Building Material,* 262: 120737. doi: 10.1016/j.conbuildmat.2020.120737.

[10] N. Rozman *et al.*, 2021 "TiO_2 photocatalyst with single and dual noble metal co-catalysts for efficient water splitting and organic compound removal," *International Journal Hydrogen Energy* 46(65): 32871–32881, doi: 10.1016/j.ijhydene.2021.07.129.

[11] N. Ramesh Reddy, M. Mamatha Kumari, K. K. Cheralathan, and M. V. Shankar, 2018 "Enhanced photocatalytic hydrogen production activity of noble metal free MWCNT-TiO_2 nanocomposites," *International Journal Hydrogen Energy* 43(8): 4036–4043, doi: 10.1016/j.ijhydene.2018.01.011.

[12] V. Navakoteswara Rao *et al.*, 2021, "Metal chalcogenide-based core/shell photocatalysts for solar hydrogen production: Recent advances, properties and technology challenges," *Journal Hazardous Material*, 415: 125588, doi: 10.1016/j.jhazmat.2021.125588.

[13] R. A. Hussain and I. Hussain, 2019, "Fabrication and applications of nickel selenide," *Journal of Solid State Chemestry.*, 277: 316–328, doi: 10.1016/j.jssc.2019.06.015.

[14] X. Jiang, H. Gong, Q. Liu, M. Song, and C. Huang, 2020, "In situ construction of NiSe/Mn0.5Cd0.5S composites for enhanced photocatalytic hydrogen production under visible light," *Applied Catalyst B Environment.*, 268: 118439, doi: 10.1016/j.apcatb.2019.118439.

[15] H. Gong, Q. Liu, and C. Huang, 2019 "NiSe as an effective co-catalyst coupled with TiO_2 for enhanced photocatalytic hydrogen evolution," *International Journal Hydrogen Energy*, 44(10): 4821–4831, doi: 10.1016/j.ijhydene.2019.01.039.

[16] A. Khan, M. Goepel, J. C. Colmenares, and R. Gläser, 2020, "Chitosan-Based N-Doped Carbon Materials for Electrocatalytic and Photocatalytic Applications," *ACS Sustainable Chemistry Engineering*, 8(12): 4708–4727, doi: 10.1021/acssuschemeng.9b07522.

[17] E. Santoso, R. Ediati, Y. Kusumawati, H. Bahruji, D. O. Sulistiono, and D. Prasetyoko, 2020, "Review on recent advances of carbon based adsorbent for methylene blue removal from waste water," *Material Today Chemistry*, 16. doi: 10.1016/j.mtchem.2019.100233.

[18] I. Aranaz *et al.*, 2021 "Chitosan: An overview of its properties and applications," *Polymers*, 13(19) doi: 10.3390/polym13193256.

[19] M. Zeng *et al.*, 2016, "N-doped mesoporous carbons supported palladium catalysts prepared from chitosan/silica/palladium gel beads," *International Journal Biology Macromolecules*, 89: 449–455. doi: 10.1016/j.ijbiomac.2016.05.011.

[20] R. Shi *et al.*, 2018, "NaCl-templated synthesis of hierarchical porous carbon with extremely large specific surface area and improved graphitization degree for high energy density lithium ion capacitors," *Journal Material Chemistry A*, 6(35): 17057–17066, doi: 10.1039/c8ta05853a.

[21] Q. Wu *et al.*, 2019, "N-doped porous carbon from different nitrogen sources for high-performance supercapacitors and CO_2 adsorption," *Journal of Alloys Compounds*, 786: 826–838. doi: 10.1016/j.jallcom.2019.02.052.

[22] J. Ding, P. Wang, S. Ji, H. Wang, D. J. L. Brett, and R. Wang, 2019, "Mesoporous nickel selenide N-doped carbon as a robust electrocatalyst for overall water splitting," *Electrochimica Acta*, 300: 93–101. doi: 10.1016/j.electacta.2019.01.093.

[23] L. Zheng, S. Han, H. Liu, P. Yu, and X. Fang, 2016. "Hierarchical MoS2 Nanosheet@TiO_2 Nanotube Array Composites with Enhanced Photocatalytic and Photocurrent Performances," *Small*, 12(11): 1527–1536, doi: 10.1002/smll.201503441.

[24] Z. Zhang, Z. Zhou, H. Peng, Y. Qin, and G. Li, 2014 "Nitrogen- and oxygen-containing hierarchical porous carbon frameworks for high-performance supercapacitors," *Electrochimica Acta*, 134: 471–477. doi: 10.1016/j.electacta.2014.04.107.

[25] A. J. Alabdulghani, 2016. "Novel Techniques to Characterize Pore Size of Porous Materials,"

[26] Y. Liu *et al.*, 2023, "NaCl-assisted synthesis of porous carbons with ultra-high electrical conductivity for high-performance supercapacitors," *Journal of Power Sources*, 553 doi: 10.1016/j.jpowsour.2022.232301.

[27] N. Moloto, M. J. Moloto, N. J. Coville, and S. Sinha Ray, 2009. "Optical and structural characterization of nickel selenide nanoparticles synthesized by simple methods," *Journal of Crystal Growth*, 311(15): 3924–3932. doi: 10.1016/j.jcrysgro.2009.06.006.

[28] M. S. Begum and A. J. Ahamed, 2015. "Synthesis and characterization of NiSe and Doped NiSe: Mn," 9,

[29] D. P. Rahmadani, A. Rahmada, F. Marendra, H. J. Rimbawan, R. B. Cahyono, and T. Ariyanto, 2021. "Biogas Purification Using Chitosan-Impregnated Porous Carbon,"

[30] K. Osler, N. Twala, O. O. Oluwasina, and M. O. Daramola, 2017. "Synthesis and Performance Evaluation of Chitosan/Carbon Nanotube (Chitosan/MWCNT) Composite Adsorbent for Post-combustion Carbon Dioxide Capture," in *Energy Procedia*, Elsevier Ltd. 2330–2335. doi: 10.1016/j.egypro.2017.03.1368.

[31] P. Praveen, G. Viruthagiri, S. Mugundan, and N. Shanmugam, 2014, "Structural, optical and morphological analyses of pristine titanium di-oxide nanoparticles – Synthesized via sol–gel route," *Spectrochimia Acta Part A: Molecular Biomolecular Spectroscopy*, 117: 622–629 doi: 10.1016/j.saa.2013.09.037.

[32] J. Yu and J. Ran, 2011, "Facile preparation and enhanced photocatalytic H_2-production activity of $Cu(OH)_2$ cluster modified TiO_2," *Energy and Environmental Science* 4(4): 1364–1371. doi: 10.1039/c0ee00729c.